High order modes of intense second harmonic light produced from a plasma aperture

View Online   Export Citation   CrossMark

E. F. J. Bacon,[1] M. King,[1,2] R. Wilson,[1] (iD) T. P. Frazer,[1,2] R. J. Gray,[1] (iD) and P. McKenna[1,2a] (iD)

AFFILIATIONS

[1] SUPA Department of Physics, University of Strathclyde, Glasgow G4 0NG, United Kingdom
[2] The Cockcroft Institute, Sci-Tech Daresbury, Warrington WA4 4AD, United Kingdom

Note: This paper is a part of the Special Topic Collection on Plasma Optics.
[a] Author to whom correspondence should be addressed: paul.mckenna@strath.ac.uk

ABSTRACT

Because of their ability to sustain extremely high-amplitude electromagnetic fields and transient density and field profiles, plasma optical components are being developed to amplify, compress, and condition high-power laser pulses. We recently demonstrated the potential to use a relativistic plasma aperture—produced during the interaction of a high-power laser pulse with an ultrathin foil target—to tailor the spatiotemporal properties of the intense fundamental and second-harmonic light generated [Duff *et al.*, Sci. Rep. **10**, 105 (2020)]. Herein, we explore numerically the interaction of an intense laser pulse with a preformed aperture target to generate second-harmonic laser light with higher-order spatial modes. The maximum generation efficiency is found for an aperture diameter close to the full width at half maximum of the laser focus and for a micrometer-scale target thickness. The spatial mode generated is shown to depend strongly on the polarization of the drive laser pulse, which enables changing between a linearly polarized TEM_{01} mode and a circularly polarized Laguerre–Gaussian LG_{01} mode. This demonstrates the use of a plasma aperture to generate intense higher-frequency light with selectable spatial mode structure.

I. INTRODUCTION

The ability to manipulate light at relativistic intensities[1] ($>10^{18}$ W cm^{-2} for a laser wavelength of ~1 μm) is an important aspect of the development of compact laser-driven particle and radiation sources.[2,3] Such sources have wide-ranging potential applications including medicine,[4–6] ultrafast imaging,[7] industrial processing,[8] and inertial confinement fusion.[9,10] Tailoring the spatial and temporal profile of the laser pulse can be used to optimize focusing behavior in laser–plasma interactions,[11] which can enhance laser-driven particle acceleration[12,13] and has the potential to produce radiation sources with orbital angular momentum (OAM).[14]

The conventional approach to manipulating light is based on using solid-state optical media, but there is a limit to the energy density that these media can withstand before nonlinear effects distort the laser pulse and the optics themselves are damaged. This is typically circumvented by increasing the size of the optics as the laser energy is increased so that the overall energy density is below the critical value. However, large-area optics are very expensive, with long manufacture times and limited maneuverability because

of their volume and weight. By contrast, plasma optical components are inherently compact, easily achieving energy densities of more than two orders of magnitude higher. In addition, the ultrafast evolution of the optical properties of laser-excited plasma enables other properties of the laser pulse to be tailored. By using plasma-based optics, it is possible to enhance the temporal intensity contrast of the laser pulse,[15–17] refocus it to enhance the laser peak intensity significantly,[18–20] compress its temporal profile,[21] generate high harmonics,[22–24] and amplify the pulse.[25–27] Through the interaction of intense light with dense plasma oscillations, the production of transient plasma gratings,[28–30] holograms,[31] and coherent emission of light[32] can also be achieved.

In recent studies involving intense laser-pulse interactions with ultrathin (tens of nanometers) foils, we introduced the concept of a self-generated *relativistic plasma aperture* that enables the laser light to pass through a region of an initially opaque target, resulting in diffraction and manipulation of the particle dynamics in the corresponding field structures.[33,34] This plasma aperture forms because a region of the target becomes relativistically transparent[35] to the laser light, which occurs when the plasma frequency ω_p

$[= \sqrt{n_e e^2/(\gamma \epsilon_0 m_e)}$, where n_e is the electron density, e is the electron charge, γ is the electron Lorentz factor, ϵ_0 is the permittivity of free space, and m_e is the electron rest mass] is reduced to below the laser frequency ω_L. The electron density at which this occurs is known as the relativistically corrected critical density γn_{crit}, and at currently achievable laser intensities, the process is aided by target heating and expansion reducing the peak electron density in the focal-spot region. As relativistically induced transparency occurs above an intensity threshold, the spatial profile for a Gaussian focal spot is circular, forming a relativistic plasma aperture in the target.[33] As the transmitted portion of the laser pulse interacts with the edge of this plasma aperture, intense light is generated at ω_L and $2\omega_L$ with higher-order transverse spatial mode structures and different polarization states compared with the drive laser pulse.[36] An example result from a 3D particle-in-cell (PIC) simulation of the interaction of an intense pulse with an initially solid-density 10-nm-thick aluminum target is shown in Fig. 1(a), in which can be seen
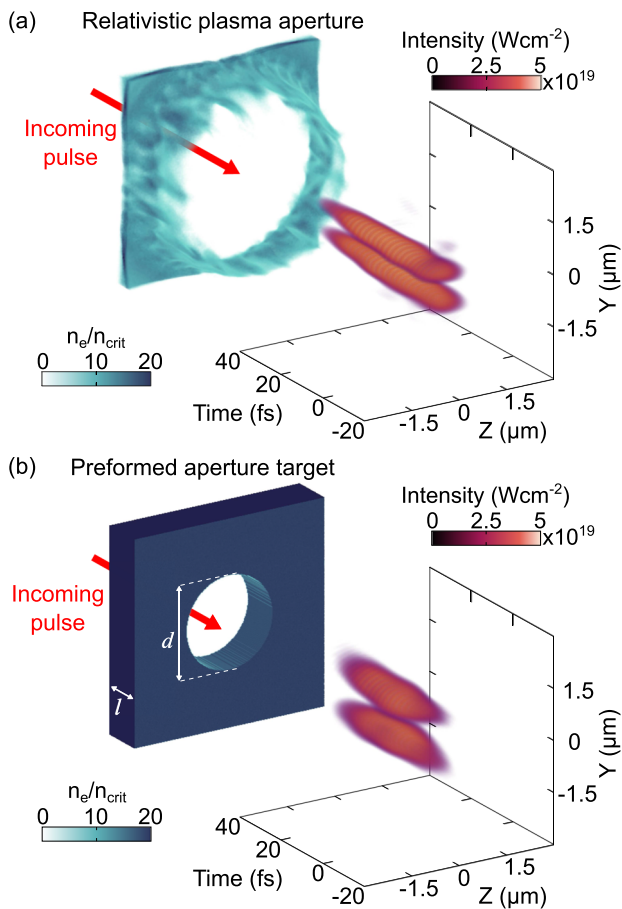

FIG. 1. Example 3D simulation results demonstrating the generation of relativistically intense frequency-doubled light in a higher-order spatial mode (TEM$_{01}$) driven by intense laser light in a fundamental TEM$_{00}$ mode: (a) self-generated relativistic plasma aperture in an initially solid-density 10-nm-thick aluminum target; (b) preformed aperture target with thickness $l = 2$ μm and aperture diameter $d = 3$ μm.

the self-generated relativistic plasma aperture and $2\omega_L$ light emitted in the TEM$_{01}$ mode. This was driven by a linearly polarized (in Y) 6-J, 40-fs-duration laser pulse focused to a peak intensity of 6×10^{20} W cm^{-2}, in a fundamental TEM$_{00}$ mode; see Duff *et al.*[36] for a full description of the high-order spatial mode generation mechanism. When the incoming laser light is circularly polarized, light with OAM can be produced at the higher harmonics of the laser frequency.[37]

The laser–plasma-aperture interaction effectively acts to transfer energy from the incoming laser pulse—which has a fundamental Gaussian spatial mode structure—to intense harmonic light in higher-order modes. This could potentially be developed as a plasma optical device. Although the use of ultrathin targets is challenging because of their fragility, which can limit the shot repetition rate, the scheme could potentially be simplified by using micrometer-thick targets incorporating a preformed circular aperture to produce the same effect.[36] This is illustrated in Fig. 1(b), which is an example 3D simulation result showing the generation of relativistically intense $2\omega_L$ light in the TEM$_{01}$ mode in a target with thickness $l = 2$ μm and aperture diameter $d = 3$ μm. These targets could then also be used as a platform to test more readily the underlying physics that occurs during the formation of a relativistic plasma aperture.

Herein, we investigate the potential use of preformed-aperture targets for generating frequency-doubled light with higher-order spatial mode structures. Using 2D and 3D PIC simulations, we determine the optimum target parameters to maximize the efficiency of energy transfer, and we show that this is related to the fraction of light transmitted through the aperture, the strength of the longitudinal electric field at the aperture edge, and the absorption of the laser pulse. Using 3D simulations, we compare the generation efficiency and mode structure formation when the polarization is varied from linear to circular. The results highlight the feasibility of using a preformed-aperture target—resulting in a plasma aperture—as a type of plasma optical device for mode conversion of intense light.

II. METHODS

To investigate and optimize the generation of frequency-doubled light in higher-order spatial modes, 2D and 3D simulations were performed using the fully relativistic PIC code EPOCH.[38] For the 2D case, the simulation XY grid was defined as 1000×720 mesh cells, corresponding to 20×20 μm^2. For the 3D simulations, the XYZ grid was defined as $1000 \times 720 \times 720$ cells, corresponding to $20 \times 20 \times 20$ μm^3. The targets comprised a slab of Al^{13+} ions of thickness l with a circular aperture of diameter d. This was neutralized with an electron population with a peak density of $30n_{crit}$ and an initial temperature of 10 keV. Each species was initialized with an average of 80 particles per cell in the 2D case and five particles per cell in the 3D case. All the boundaries of the simulation box were defined as free-space ones, and the ions were mobile in all cases.

In both the 2D and 3D simulations, the pulse of laser light with wavelength $\lambda_L = 800$ nm entering from the left (X) boundary and was focused at the plane corresponding to the front surface of the target ($X = 0$). Both the laser-pulse temporal and spatial profiles were defined in terms of intensity as Gaussian with pulse duration $\tau_L = 40$ fs [full width at half maximum (FWHM)] and focal-spot diameter $\phi_L = 2.1$ μm (FWHM). Time $t = 0$ was defined as when the peak of the pulse reached the front surface of the

target, i.e., the front of the aperture. The 3D simulations were performed using linear polarization in the Y direction and circular polarization. In the 2D simulations, only linear polarization in the Y direction was used because circular polarization cannot interact with the full aperture edge. The peak laser-pulse intensity I_L was varied from 10^{21} to 10^{23} W cm^{-2} by increasing the energy in the pulse. In the 2D simulations, a simulation automation code called BISHOP[39]—developed by our group—was used to systematically scan a 2D parameter grid of target thickness and aperture diameter; l was varied from 0.5 to 10 μm and d was varied from 0.5 to 5 μm.

III. RESULTS

A. 2D simulations

Figure 2(a) shows the electron density for a target with l = 0.5 μm at t = −4.8 fs from a 2D simulation, demonstrating the generation of electron bunches from the predefined (d = 3 μm) aperture edges as the laser interacts and propagates through; at each side, the electron bunches are emitted with frequency ω_L, π out of phase with the opposite side (because of the oscillation of the laser electric field vector), with an overall frequency of $2\omega_L$ when considering the bunches from both sides of the aperture. Figure 2(b) shows an

example 2D map of the longitudinal electric field 6 fs thereafter; the pattern is produced by the interference from the two point sources at the opposite edges of the aperture. To investigate the temporal generation of $2\omega_L$ light, an arbitrary electron bunch—circled in Fig. 2(a) with its corresponding position shown 6 fs later in Fig. 2(b)—is tracked through the simulation. In Fig. 2(c), the total kinetic energy K_e in the bunch is plotted as a function of X (the axis of laser propagation), together with the generated $2\omega_L$ intensity $I_{2\omega L}$ and the longitudinal electric field experienced E_X (both averaged 400 nm around the bunch). The electron bunch is accelerated immediately to relativistic velocities from the aperture edge, before experiencing a decelerating longitudinal electric field as it propagates with the laser and into the sheath field at the target rear (formed because of the charge separation of earlier fast electrons and rear surface plasma surrounding the aperture[40,41]). This can be observed in Fig. 2(b) as the overall positive electric field (in the positive X direction) at the rear of the target, together with the longitudinal field associated with the laser pulse. Both the acceleration and deceleration of the electron bunch result in broadband emission that interferes constructively with the emission from neighboring bunches, resulting in the generation of $2\omega_L$ light. This is due to the periodic nature of the accelerated bunches produced at either side of the aperture, which have an overall frequency of $2\omega_L$. As a result of this, the intensity of the $2\omega_L$ light along the longitudinal axis increases with
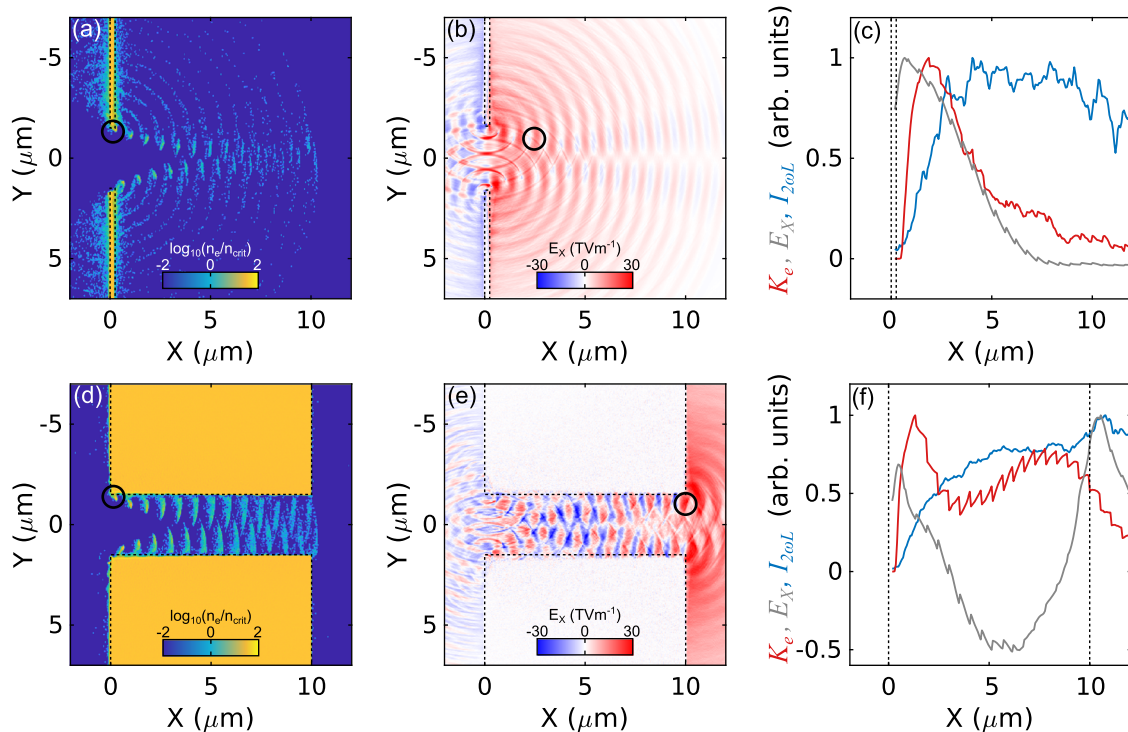

FIG. 2. Top row: 2D simulation results for a target with l = 0.5 μm and d = 3 μm: (a) electron density at t = −4.8 fs; (b) longitudinal electric field at t = 2.8 fs; (c) total energy (K_e, red) in the electron bunch marked by the black circle in (a) and (b) as it propagates in space, together with the intensity of the $2\omega_L$ light generated, averaged 400 nm around the bunch ($I_{2\omega L}$, blue), and the longitudinal electric field experienced by the bunch (E_X, grey) averaged over the same area. Bottom row: (d)–(f) show the corresponding results for l = 10 μm and d = 3 μm, with t = 28.8 fs in (e). The dashed black lines indicate the initial positions of the target surfaces and aperture edges.

distance from the aperture for ~5 μm, after which it saturates and then reduces as the generated $2\omega_L$ light expands away from the sampled region in the vicinity of the bunch.

Figures 2(d)–2(f) show the corresponding results for the case $l = 10$ μm ($d = 3$ μm), for which the aperture effectively becomes a channel. In this case, Fig. 2(e) shows the longitudinal electric field 24 fs after the electron density plot in Fig. 2(d), when the bunch has reached the rear of the target. As can be seen in Fig. 2(f), the initial acceleration of the electron bunch and generation of $2\omega_L$ light are similar to those in case of $l = 0.5$ μm. However, as the electron bunch and laser co-propagate within the extended plasma aperture/channel, the electrons experience the positive longitudinal field associated with the focused Gaussian pulse (due to the divergence of the laser electric field profile, i.e., $\nabla \cdot \vec{E} = 0$ in free space), resulting in a deceleration of the bunch. The bunch never comes to rest, and it continues to propagate in the positive X direction with a relativistic velocity at all times. As the bunch propagates, it begins to dephase with the laser pulse and experiences the negative longitudinal field associated with the subsequent half-wave period, accelerating the bunch again. In both the deceleration and acceleration phases, the electrons emit, and the constructive interference with the neighboring emission produces a strong $2\omega_L$ signal. As the bunch leaves the aperture/channel at $X = 10$ μm, it experiences the sheath field at the target rear and again decelerates, resulting in further $2\omega_L$ emission.

The aperture diameter and target thickness influence the energy conversion to $2\omega_L$. To determine the influence of these parameters, a detailed parameter scan was performed to observe the changes to the generation efficiency, based on the ratio of the total energy of the generated $2\omega_L$ light detected 5 μm from the target rear to the energy of the input laser pulse. Figure 3 shows the conversion efficiency as a function of target thickness and aperture diameter for three different laser intensities. For $I_L = 10^{21}$ W cm^{-2}, the optimal efficiency is found to be $d \sim 2$ μm, shown in Fig. 3(a) as region I. At this aperture diameter, the efficiency saturates for $l \gtrsim 6$ μm. When the aperture diameter is increased, the edges of the aperture experience less interaction with the longitudinal field of the laser pulse and the efficiency of $2\omega_L$ thus reduces, as observed in region II.

Region III indicates that for small d, the efficiency decreases with increasing l. This is due to poor matching conditions between the free-space Gaussian laser beam focus and the close-to-cut-off modes that can exist within the aperture when the thickness is increased beyond the wavelength; this acts to attenuate the beam

within the aperture. As d is reduced from the optimal at 2 μm (for the 2.1-μm FWHM laser focal spot), the generation efficiency therefore becomes very dependent on l. For the thickest targets, the efficiency reduces to negligible levels because the beam is attenuated greatly. However, reducing l enables appreciable efficiency to be regained, as indicated by region IV. This is due to the aperture evolving with the laser pulse. While small apertures inhibit the propagation of laser light because of poor matching conditions, the transverse ponderomotive force of the focused light is intense enough to expel the plasma from the focal-spot region. If the target is thin enough, this expulsion is sufficient to increase the size of the aperture and continue to generate $2\omega_L$ light, similar to that of the interaction with an ultrathin foil target as reported by Duff et al.[36] This effect can be observed more readily as the peak intensity is increased. At $I_L = 10^{22}$ W cm^{-2}, as shown in Fig. 3(b), the generation efficiency for the smallest d occurs over a much larger l range, and region IV widens in the 2D parameter map. As the intensity is increased further to $I_L = 10^{23}$ W cm^{-2}, as shown in Fig. 3(c), region IV becomes broad across the entire d and l ranges, resulting in no observable region III. This effect is likely to be exaggerated by the reduced peak density (in comparison to the solid density of ~430n_{crit}) used in the simulations. In this scenario, I_L is high enough at the edges of the aperture that the heating of the plasma by the laser is sufficient for the interaction region to become relativistically transparent near the peak of the pulse, regardless of d. This acts to reduce the efficiency of the generation mechanism because the effective aperture diameter is now much larger than the starting value, in all cases. The optimal condition at $d \sim 2$ μm still exists because the rising edge of the laser pulse (with less intensity) still interacts with the initial aperture diameter.

B. Efficiency modeling

Next, we explore the observed dependence of the $2\omega_L$ generation efficiency on d and l. It is shown above that during the interaction of the laser pulse with the aperture edge, the longitudinal electric field acts to accelerate and decelerate the bunched electrons. It is therefore assumed that the magnitude of the field close to the aperture edge plays a role in defining the efficiency of $2\omega_L$ generation. The longitudinal electric field for a pulse with a focused Gaussian spatial profile can be determined from the spatial differential of the electric field along the polarization direction. The maximum absolute value of this field is at a transverse position of
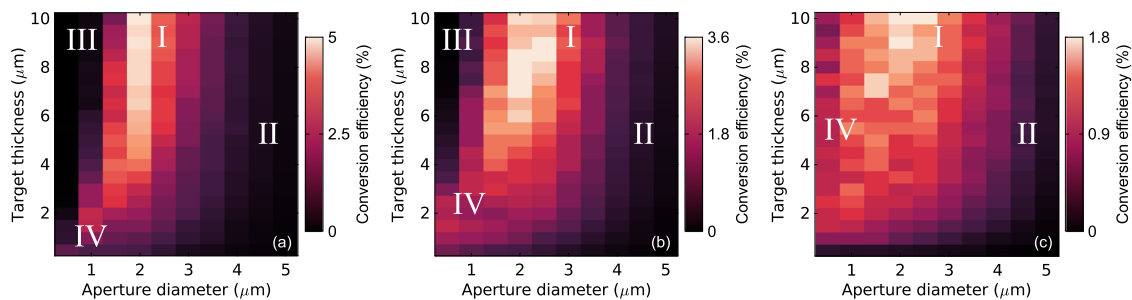

FIG. 3. 2D simulation results showing the efficiency of $2\omega_L$ light generation as a function of target thickness and aperture diameter, after the interaction of a linearly polarized laser pulse with an intensity of: (a) 10^{21} W cm^{-2}; (b) 10^{22} W cm^{-2}; and (c) 10^{23} W cm^{-2}. All of the other laser parameters are fixed. The regions of behavior indicated by the Roman numerals are discussed in the main text.
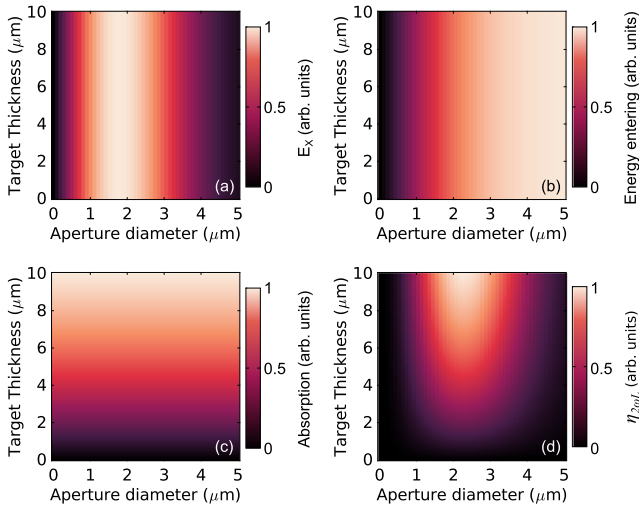
FIG. 4. Three parameters that vary with both target thickness and aperture diameter, for the interaction with a 10^{21} W cm^{-2} laser pulse: (a) magnitude of the longitudinal electric field at the aperture edge; (b) the energy into the aperture; (c) the laser absorption. (d) Conversion efficiency to $2\omega_L$, as defined by Eq. (4).

$Y \sim \phi_L/2$. As such, as d is increased, the magnitude of this longitudinal electric field at the aperture edge, E_X, is maximized when $d \sim \phi_L$; this is shown in Fig. 4(a). For a pulse that is linearly polarized in the Y dimension, E_X is defined as

$$E_X(Y) = \frac{d}{dY} e^{-\left(\frac{2\sqrt{\ln(2)}Y}{\phi_L}\right)^2}. \tag{1}$$

The fraction of the laser light that can enter the aperture is another factor that influences $2\omega_L$ generation. The greater the energy that can propagate through the aperture, the greater the potential conversion into second-harmonic light. The energy in the pulse that can enter the aperture, K_{in}, is shown in Fig. 4(b) for the 2D simulations and is given by

$$K_{in}(d) = \int_{-d/2}^{d/2} e^{-\left(\frac{2\sqrt{\ln(2)}Y}{\phi_L}\right)^2} dY. \tag{2}$$

This varies with d because more of the laser pulse is blocked for smaller apertures. As I_L is increased, relativistic transparency at the aperture edges can occur, enabling more light to enter, but this is a second-order effect and is not included in this simple model.

A third parameter influencing conversion to $2\omega_L$ light is the overall absorption of the energy of the laser pulse into the electron bunches, Abs_L, as it propagates through the aperture. We assume that this varies linearly with l with an absorption coefficient α because the number of electrons exposed to the propagating laser pulse increases with l. We also assume an exponential attenuation of the laser pulse with thickness with an attenuation constant β. Because the actual attenuation of the laser pulse is complicated by effects such as self-focusing and reflection, the attenuation constant is treated as a free parameter, approximated based on the level of

transmitted light in the simulation results ($\beta = 0.1$). This is shown in Fig. 4(c), and the overall absorption is given as

$$Abs_L(l) = \alpha l e^{-\beta l}. \tag{3}$$

Assuming that these parameters are related linearly gives the following first-order approximate relationship for the $2\omega_L$ conversion efficiency $\eta_{2\omega_L}$:

$$\eta_{2\omega_L} \propto |E_X(d/2)| Abs_L(l) K_{in}(d). \tag{4}$$

The variation of this relationship with d and l is plotted in Fig. 4(d), which matches well with the simulation results in Fig. 3. This simple model is useful only to demonstrate the behavioral trend of the conversion efficiency. Factors such as relativistic transparency and the reabsorption of $2\omega_L$ generated light are not included: relativistic transparency will affect only the thinnest targets and the highest-intensity pulses, and the reabsorption of $2\omega_L$ light will become significant only for very thick targets.

C. 3D simulations

Because harmonic light from the plasma aperture can be produced in non-symmetric modes,[36,37] it is necessary to extend the investigation to include 3D simulations. Because of the substantially increased computational requirements in doing so, a reduced set of simulations was performed to check whether the efficiency dependencies observed in 2D are the same in 3D. The results are presented in Fig. 5(a). The overall trends in the dependencies on l and d are similar to the 2D results, noting that the maximum conversion efficiency is reduced to ~3.5% and the optimal d is found to be slightly larger at 3 ± 0.5 μm (compared to 2 μm for 2D). The reduction in
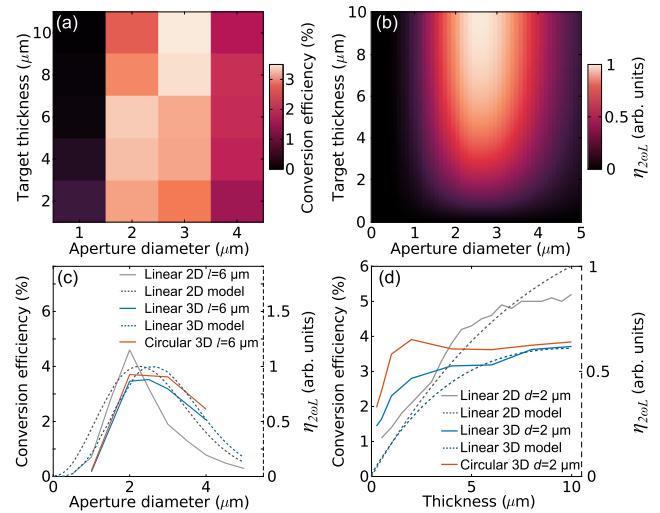

FIG. 5. 3D simulation results. (a) $2\omega_L$ generation efficiency as a function of d and l. (b) Conversion efficiency as given by Eq. (4) for 3D conditions. (c) and (d) $2\omega_L$ generation efficiency as a function of (c) d for $l = 6$ μm, and (d) l for $d = 3$ μm. 3D linear polarization results are shown in blue and circular polarization results are shown in orange. 2D simulation data are included for comparison (dashed black line) for fixed $l = 6$ μm and $d = 2$ μm in (c) and (d), respectively. $I_L = 10^{21}$ W cm^{-2} for all cases.

conversion efficiency is likely due to the fact that in 2D, the intensity is simulated only in the plane of the laser polarization where the polarization vector is perfectly normal to the aperture edge. In 3D, there is no significant interaction when the polarization vector is parallel to the aperture edge, resulting in proportionally less energy available to produce $2\omega_L$ light. The additional degree of freedom also means that the accelerated electrons are less confined to the laser field as they propagate. The total area of the laser focus, as well as the area of the aperture, must be considered in 3D, which modifies Eq. (3) as follows:

$$K_{in}(d) = \int_{-\pi}^{\pi} \int_0^{d/2} e^{-\left(\frac{2\sqrt{\ln(2)}r}{\phi_L}\right)^2} r \, dr \, d\phi, \qquad (5)$$

where the integral is given in cylindrical coordinates. Figure 5(b) shows the calculated $\eta_{2\omega_L}$ with Eq. (5) used to account for the changes in 3D. This results in an increase of the optimal d by ~0.5 μm.

For a direct comparison of the dependencies of $\eta_{2\omega_L}$ on d and l in 2D and 3D, line-outs from both sets of simulation results are presented in Fig. 5(c) for fixed $l = 10\,\mu$m and Fig. 5(d) for fixed $d = 2\,\mu$m in 2D and $d = 3\,\mu$m in 3D (i.e., the optimum diameter in each case). The model calculations based on the approximate conversion relationships are also shown for the 2D and 3D cases and are found to be in good overall agreement with the trends observed in the simulation results.

The 2D and 3D simulation results exhibit similar overall trends. The efficiency increases rapidly with d to an optimum value, and as the aperture size is increased beyond this, $\eta_{2\omega_L}$ decreases more slowly
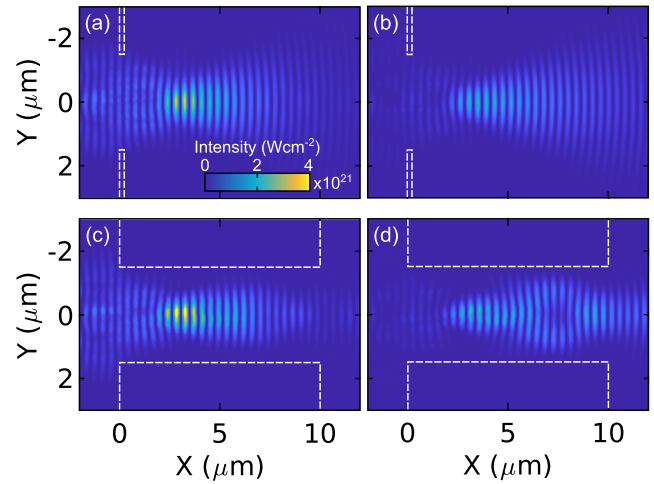

FIG. 6. Intensity profile of the drive laser light in the XY plane at $Z = 0$ from 3D simulations, for $d = 3\,\mu$m and $l = 0.25\,\mu$m, at: (a) $t = 16$ fs and (b) $t = 32$ fs. (c) and (d) are the corresponding results for $l = 10\,\mu$m. The dashed white lines indicate the initial target profile, and the nominal focused intensity (without plasma) is 10^{21} W cm^{-2} in both cases.

with d in the 3D case. The optimum d is also ~0.5 μm higher in 3D, as predicted by the simple model. As l is varied (for the optimal d), the efficiency rises slightly faster in the 3D case compared to the corresponding results in 2D, before saturating at ~3.5%. These discrepancies may be due to the optimal d being slightly larger in the 3D
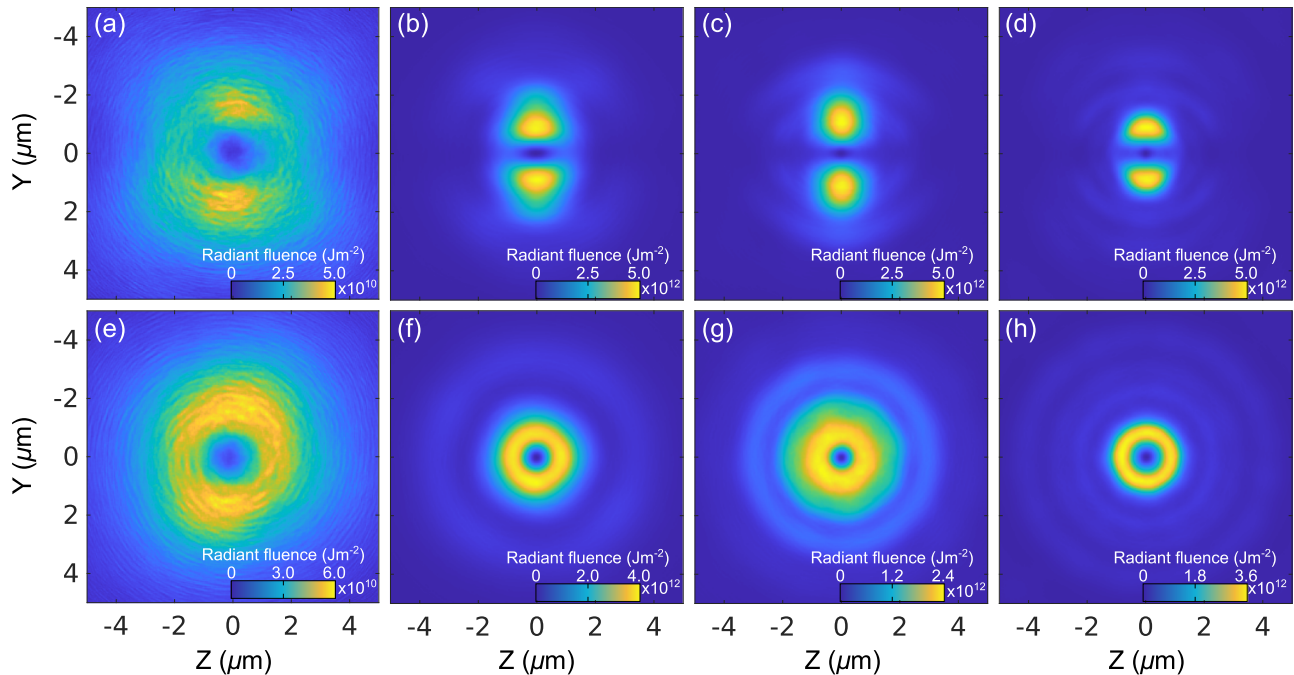

FIG. 7. Time-integrated spatial mode structure at 5 μm from the rear of the target. Top row: linear polarization and $d =$ (a) 1 μm, (b) 2 μm, (c) 3 μm, and (d) 4 μm, all for $l = 6\,\mu$m. Bottom row: corresponding results with circular polarization, with otherwise the same laser and target parameters.

case. As the laser pulse expands after focus, the intensity decreases as r^2 in 3D compared to r in 2D, which will change the effective intensity. Second-order effects such as self-focusing[42,43] and reflection of the laser pulse as it moves through the aperture may also induce discrepancies between 2D and 3D, because these process can change the intensity and longitudinal electric field.

To illustrate the self-focusing and scalloping behavior in the plasma aperture, Fig. 6 shows the laser intensity profile of the drive laser pulse in two example targets with differing l.

Figures 6(a) and 6(b) show the ω_L intensity profile in the XY plane along $Z = 0$ from the 3D simulations for $l = 0.5$ μm at example times $t = 16$ and 32 fs, respectively. The laser pulse is observed to experience self-focusing as it passes through the aperture to a position of $X \approx 2.5$ μm before expanding out into free space. Note that the intensity increases from the nominal intensity of 1×10^{21} W cm^{-2} (without plasma) to $\sim 4 \times 10^{21}$ W cm^{-2}. This is twice as high as can be achieved with the same focus in the 2D simulations because of dimensionality effects (the pulse energy can be focused only in a plane in 2D but radially in 3D). When l is increased to 10 μm, as shown for the same example times in Figs. 6(c) and 6(d), the self-focusing behavior is very similar, but the expansion is inhibited by the extended aperture/channel in this case, resulting in scalloping behavior. At the later time step [Fig. 6(d)], the pulse is observed to have refocused toward the rear of the target.

In the 3D simulations, the spatial structure of the generated $2\omega_L$ light takes the form of a TEM$_{01}$ mode. The exact spatial distribution of the mode depends on the aperture geometry. Figures 7(a)–7(d) show the change in the mode structure as d is increased for fixed $l = 6$ μm. This is temporally integrated over the full pulse duration. For the smallest aperture ($d = 1$ μm), low levels of $2\omega_L$ light are generated (note the change in fluence scale) but the TEM$_{01}$ mode is still observed. As d is increased, the mode structure becomes very clear and the overall beam size is observed to reduce. As the aperture size is increased, there are also low amounts of $2\omega_L$ light produced outside of this central mode, with even higher-order structures. This is caused by the interference of the generated light varying as the sources are moved farther apart.[37] These can be seen more readily on a logarithmic scale, as shown in Fig. 8(a).

D. Polarization effects

All the simulation results discussed thus far involve linear polarization. When the drive laser pulse is circularly polarized, high harmonic light is produced with a Laguerre–Gaussian (LG) mode structure.[37] To explore the effect of polarization on the $2\omega_L$ conversion efficiency, a further subset of simulations was also performed for circularly polarized drive laser light. In this case, the peak intensity was halved to maintain the same pulse energy as in the linear pulse case.

Figures 5(c) and 5(d) show the conversion efficiency as a function of d and l with circular polarization for the same fixed parameters as in the linear cases. The overall trends are similar to the linear polarization cases, but with a general increase in overall efficiency in conversion to $2\omega_L$ light. This is due to the polarization vector always being normal to the aperture edge in the case of circular polarization, resulting in $2\omega_L$ light being produced over the entire wave period.

Figures 7(e)–7(h) show the variation in spatial distribution of the temporally integrated $2\omega_L$ light for circular polarization as d is varied. The generated mode takes the form of a ring distribution,[37] as expected from an LG mode. Similar to the linear polarization case, the aperture diameter affects the size of the main central ring and low-level higher-order ring-like distributions are evident as separation of the electron bunches increases (i.e., with increasing d), resulting in a change to the interference pattern. This is seen more clearly on the logarithmic scale in Fig. 8(b).

E. Effects of temporal intensity contrast

In practice, depending on the temporal intensity contrast of the laser pulse, some degree of ionization and expansion of the target may be induced early in the interaction, prior to the arrival of the main pulse. Various techniques can be applied to improve the contrast of the pulse, including using plasma mirrors,[15–17] but depending on the final intensity profile of the leading edge of the laser pulse, preplasma may still be generated, resulting in an expansion of plasma toward the center of the aperture. This will result in a reduction of the effective aperture diameter as the critical surface moves inward, causing the $2\omega_L$ light generation to have the characteristics of that produced by a smaller-aperture target.

The rising edge of the laser may also produce a degree of underdense plasma within the aperture, which may affect how the laser pulse propagates. To test the impact of this, a series of 3D simulations was conducted in which the inside of a $d = 3$ μm, $l = 6$ μm aperture target was filled with plasma of varying density. Figure 9(a) shows the influence of this on the efficiency of conversion to $2\omega_L$ light. For densities less than $0.1n_{crit}$, there is very little (a few percent) reduction in conversion efficiency. The reduction is more significant at higher densities ($\sim 60\%$ at n_{crit}), but the targets are not expected to be used under a temporal intensity contrast so low as to induce such a closure of the aperture. A full investigation of this would require 3D magnetohydrodynamic simulations, which are beyond the present scope.
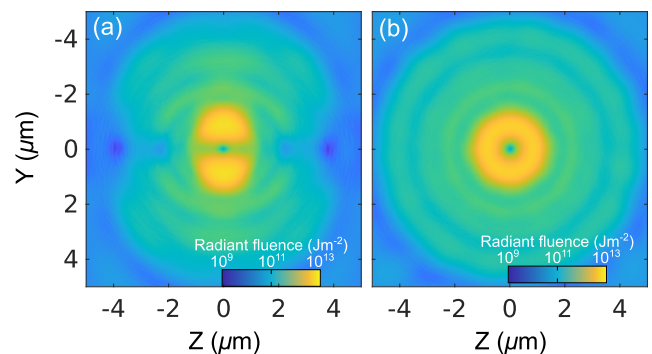

FIG. 8. Time-integrated spatial mode structure at 5 μm from the rear of the target with $d = 4$ μm, for (a) linear polarization and (b) circular polarization. The data are the same as those in Figs. 7(d) and 7(h), respectively, with fluence plotted on a logarithmic scale to show the higher-order spatial structures present at larger radii.
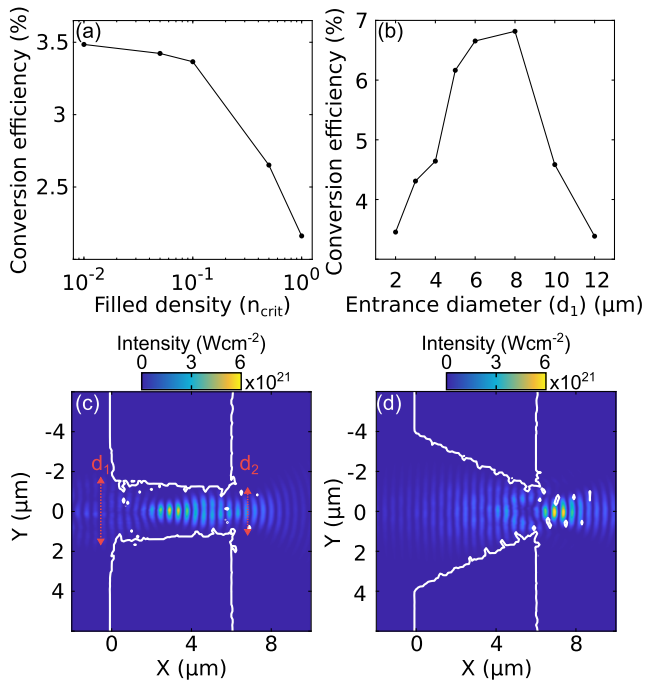
FIG. 9. (a) Conversion efficiency to $2\omega_L$ light as a function of the plasma density within the aperture, for a $d = 2~\mu m$, $L = 6~\mu m$ target. (b) Conversion efficiency to $2\omega_L$ as a function of the entrance diameter d_1, for a fixed exit diameter $d_2 = 2~\mu m$ and $l = 6~\mu m$. (c) Intensity profile of the drive laser light in the XY plane at $Z = 0$, from 3D simulations, for $d_1 = 3~\mu m$ ($d_2 = 2~\mu m$ and $l = 6~\mu m$) at $t = 23$ fs. (d) Same as (c) for $d_1 = 8~\mu m$.

F. Effects of tapering the aperture

The results presented so far involve targets for which the entrance and exit apertures are the same size, creating a parallel channel in cases with a large thickness-to-diameter ratio. It is possible to optimize the $2\omega_L$ light generation further by shaping the target geometry to control the self-focusing of the laser pulse. An additional series of 3D simulations was run in which the walls of the channel created within the aperture were angled (forming a conical target) by defining different entrance and exit diameters d_1 and d_2, respectively. Figure 9(b) shows the efficiency of conversion to $2\omega_L$ light as a function of d_1 for fixed $l = 6~\mu m$ and $d_2 = 2~\mu m$. The conversion efficiency is improved by increasing the size of the entrance diameter, reaching a maximum of ~6.9% for an optimum $d_1 = 8~\mu m$. The optimum occurs when the convergence angle of the laser undergoing self-focusing matches the angle of the cone walls. This can be seen readily when comparing Figs. 9(c) and 9(d). For the case $d_1 = 3~\mu m$ [Fig. 9(c)], self-focusing of the propagating light results in a focal position inside the target, similar to Fig. 6(c). For $d_1 = 8~\mu m$, the propagating laser light self-focuses close to the exit aperture. For higher d_1, the focal position moves increasingly beyond the exit aperture and the laser pulse interacts with a shorter length of plasma wall, because the laser pulse needs to propagate deep within the aperture before interacting with it. It may be possible to tailor the geometry of these targets further to improve the conversion efficiency, and the optimum may also depend on the temporal intensity contrast of the laser pulse.

IV. CONCLUSIONS

Following our previous work on the self-generation of a relativistic plasma aperture during the interaction of intense laser light with an ultrathin foil[33] and the resultant harmonic generation in higher-order spatial modes,[36] we have performed a numerical investigation to explore the use of a preformed plasma aperture to achieve a similar output with a simpler target. The results showed that incoming laser light in a fundamental TEM$_{00}$ mode is converted to relativistically intense second-harmonic radiation emission in higher-order modes. The efficiency of conversion was explored as a function of aperture diameter and target thickness, and it was found that there is an optimal diameter at which the conversion efficiency saturates with increasing thickness. This was shown to be proportional to the intensity of light that can enter the aperture, the strength of the longitudinal electric field at the aperture edge, and the absorption of the laser energy. This study was performed for linear polarization in both 2D and 3D, which overall exhibit the same trends, allowing a multi-dimensional parameter space to be explored more readily using computationally efficient 2D simulations. Extension to circular polarization in 3D produced broadly similar trends in conversion efficiency.

For the parameter range explored, the optimum target conditions for generating $2\omega_L$ light in the TEM$_{01}$ mode yielded a conversion efficiency of ~6.9%, while the optimal efficiency for generating a $2\omega_L$ LG mode was found to be ~4%. There is potential for this to be increased further by tuning the profile of the tapered targets. As the intensity of the input pulse is increased, the efficiency is reduced slightly, but conversion efficiency of this order still produces $2\omega_L$ light that is sufficiently intense to induce highly relativistic plasma oscillations. It has also been shown that there is scope for tuning the size of the mode structure and the mode order by varying the aperture diameter. This demonstrates that a preformed-aperture target irradiated by an intense laser pulse can function as a plasma optical device for generating $2\omega_L$ light with a spatial mode structure that can be changed from non-OAM to OAM by varying the drive laser polarization.

ACKNOWLEDGMENTS

AUTHOR DECLARATIONS

Conflict of Interest

The authors have no conflicts to disclose.

Author Contributions

E. F. J. Bacon: Data curation (equal); Formal analysis (equal); Investigation (equal); Methodology (equal); Writing – original draft (equal); Writing – review & editing (equal). **M. King:** Data curation (equal); Formal analysis (equal); Investigation (equal); Methodology (equal); Supervision (equal); Visualization (equal); Writing – original draft (equal); Writing – review & editing (equal). **R. Wilson:** Data curation (equal); Formal analysis (equal); Investigation (equal); Methodology (equal); Supervision (equal); Writing – original draft (equal); Writing – review & editing (equal). **T. P. Frazer:** Investigation (equal); Methodology (equal). **R. J. Gray:** Data curation (equal); Formal analysis (equal); Investigation (equal); Methodology (equal); Project administration (equal); Supervision (equal); Writing – original draft (equal); Writing – review & editing (equal). **P. McKenna:** Conceptualization (equal); Data curation (equal); Formal analysis (equal); Funding acquisition (equal); Investigation (equal); Methodology (equal); Project administration (equal); Resources (equal); Supervision (equal); Writing – original draft (equal); Writing – review & editing (equal)

DATA AVAILABILITY

The data that support the findings of this study are openly available at https://doi.org/10.15129/823f848a-bb9c-4f84-a883-86911435f8d3.

REFERENCES

[1] G. A. Mourou, T. Tajima, and S. V. Bulanov, "Optics in the relativistic regime," Rev. Mod. Phys. **78**, 309 (2006).

[2] H. Daido, M. Nishiuchi, and A. S. Pirozhkov, "Review of laser-driven ion sources and their applications," Rep. Prog. Phys. **75**, 056401 (2012).

[3] A. Macchi, M. Borghesi, and M. Passoni, "Ion acceleration by superintense laser-plasma interaction," Rev. Mod. Phys. **85**, 751 (2013).

[4] S. V. Bulanov, T. Z. Esirkepov, V. S. Khoroshkov, A. V. Kuznetsov, and F. Pegoraro, "Oncological hadrontherapy with laser ion accelerators," Phys. Lett. A **299**, 240–247 (2002).

[5] K. Zeil, M. Baumann, E. Beyreuther, T. Burris-Mog, T. E. Cowan, W. Enghardt, L. Karsch, S. D. Kraft, L. Laschinsky, J. Metzkes *et al.*, "Dose-controlled irradiation of cancer cells with laser-accelerated proton pulses," Appl. Phys. B **110**, 437–444 (2013).

[6] F. Kroll, F.-E. Brack, C. Bernert, S. Bock, E. Bodenstein, K. Brüchner, T. E. Cowan, L. Gaus, R. Gebhardt, U. Helbig *et al.*, "Tumour irradiation in mice with a laser-accelerated proton beam," Nat. Phys. **18**, 316–322 (2022).

[7] M. Borghesi, A. Bigongiari, S. Kar, A. Macchi, L. Romagnani, P. Audebert, J. Fuchs, T. Toncian, O. Willi, S. V. Bulanov *et al.*, "Laser-driven proton acceleration: Source optimization and radiographic applications," Plasma Phys. Controlled Fusion **50**, 124040 (2008).

[8] M. Barberio, M. Sciscio, S. Vallières, F. Cardelli, S. N. Chen, G. Famulari, T. Gangolf, G. Revet, A. Schiavi, M. Senzacqua, and P. Antici, "Laser-accelerated particle beams for stress testing of materials," Nat. Commun. **9**, 372 (2018).

[9] M. Roth, T. E. Cowan, M. H. Key, S. P. Hatchett, C. Brown, W. Fountain, J. Johnson, D. M. Pennington, R. A. Snavely, S. C. Wilks *et al.*, "Fast ignition by intense laser-accelerated proton beams," Phys. Rev. Lett. **86**, 436 (2001).

[10] J. C. Fernández, B. J. Albright, F. N. Beg, M. E. Foord, B. M. Hegelich, J. J. Honrubia, M. Roth, R. B. Stephens, and L. Yin, "Fast ignition with laser-driven proton and ion beams," Nucl. Fusion **54**, 054006 (2014).

[11] E. Cormier-Michel, E. Esarey, C. G. R. Geddes, C. B. Schroeder, K. Paul, P. J. Mullowney, J. R. Cary, and W. P. Leemans, "Control of focusing fields in laser-plasma accelerators using higher-order modes," Phys. Rev. Spec. Top.–Accel. Beams **14**, 031303 (2011).

[12] J. Vieira and J. T. Mendonça, "Nonlinear laser driven donut wakefields for positron and electron acceleration," Phys. Rev. Lett. **112**, 215001 (2014).

[13] J. Vieira, J. T. Mendonça, and F. Quéré, "Optical control of the topology of laser-plasma accelerators," Phys. Rev. Lett. **121**, 054801 (2018).

[14] J. W. Wang, C. B. Schroeder, R. Li, M. Zepf, and S. G. Rykovanov, "Plasma channel undulator excited by high-order laser modes," Sci. Rep. **7**, 16884 (2017).

[15] U. Teubner, U. Wagner, and E. Förster, "Sub-10 fs gating of optical pulses," J. Phys. B: At., Mol. Opt. Phys. **34**, 2993 (2001).

[16] B. Dromey, S. Kar, M. Zepf, and P. Foster, "The plasma mirror—A subpicosecond optical switch for ultrahigh power lasers," Rev. Sci. Instrum. **75**, 645–649 (2004).

[17] G. Doumy, F. Quéré, O. Gobert, M. Perdrix, P. Martin, P. Audebert, J. C. Gauthier, J. P. Geindre, and T. Wittmann, "Complete characterization of a plasma mirror for the production of high-contrast ultraintense laser pulses," Phys. Rev. E **69**, 026402 (2004).

[18] M. Nakatsutsumi, A. Kon, S. Buffechoux, P. Audebert, J. Fuchs, and R. Kodama, "Fast focusing of short-pulse lasers by innovative plasma optics toward extreme intensity," Opt. Lett. **35**, 2314–2316 (2010).

[19] R. Wilson, M. King, R. J. Gray, D. C. Carroll, R. J. Dance, C. Armstrong, S. J. Hawkes, R. J. Clarke, D. J. Robertson, D. Neely, and P. McKenna, "Ellipsoidal plasma mirror focusing of high power laser pulses to ultra-high intensities," Phys. Plasmas **23**, 033106 (2016).

[20] R. Wilson, M. King, R. J. Gray, D. C. Carroll, R. J. Dance, N. M. H. Butler, C. Armstrong, S. J. Hawkes, R. J. Clarke, D. J. Robertson *et al.*, "Development of focusing plasma mirrors for ultraintense laser-driven particle and radiation sources," Quantum Beam Sci **2**, 1 (2018).

[21] J. Ren, W. Cheng, S. Li, and S. Suckewer, "A new method for generating ultraintense and ultrashort laser pulses," Nat. Phys. **3**, 732–736 (2007).

[22] R. Lichters, J. Meyer-ter-Vehn, and A. Pukhov, "Short-pulse laser harmonics from oscillating plasma surfaces driven at relativistic intensity," Phys. Plasmas **3**, 3425–3437 (1996).

[23] A. Tarasevitch, A. Orisch, D. von der Linde, P. Balcou, G. Rey, J.-P. Chambaret, U. Teubner, D. Klöpfel, and W. Theobald, "Generation of high-order spatially coherent harmonics from solid targets by femtosecond laser pulses," Phys. Rev. A **62**, 023816 (2000).

[24] U. Teubner, K. Eidmann, U. Wagner, U. Andiel, F. Pisani, G. D. Tsakiris, K. Witte, J. Meyer-ter-Vehn, T. Schlegel, and E. Förster, "Harmonic emission from the rear side of thin overdense foils irradiated with intense ultrashort laser pulses," Phys. Rev. Lett. **92**, 185001 (2004).

[25] G. Shvets, N. J. Fisch, A. Pukhov, and J. Meyer-ter-Vehn, "Superradiant amplification of an ultrashort laser pulse in a plasma by a counterpropagating pump," Phys. Rev. Lett. **81**, 4879 (1998).

[26] V. M. Malkin, G. Shvets, and N. J. Fisch, "Fast compression of laser beams to highly overcritical powers," Phys. Rev. Lett. **82**, 4448 (1999).

[27] R. M. G. M. Trines, F. Fiúza, R. Bingham, R. A. Fonseca, L. O. Silva, R. A. Cairns, and P. A. Norreys, "Simulations of efficient Raman amplification into the multipetawatt regime," Nat. Phys. **7**, 87–92 (2011).

[28] S. Monchocé, S. Kahaly, A. Leblanc, L. Videau, P. Combis, F. Réau, D. Garzella, P. D'Oliveira, P. Martin, and F. Quéré, "Optically controlled solid-density transient plasma gratings," Phys. Rev. Lett. **112**, 145008 (2014).

[29] Q. Chen, D. Maslarova, J. Wang, S. X. Lee, V. Horný, and D. Umstadter, "Transient relativistic plasma grating to tailor high-power laser fields, wakefield plasma waves, and electron injection," Phys. Rev. Lett. **128**, 164801 (2022).

[30] H.-C. Wu, Z.-M. Sheng, Q.-J. Zhang, Y. Cang, and J. Zhang, "Manipulating ultrashort intense laser pulses by plasma Bragg gratings," Phys. Plasmas **12**, 113103 (2005).

[31] M. R. Edwards, V. R. Munirov, A. Singh, N. M. Fasano, E. Kur, N. Lemos, J. M. Mikhailova, J. S. Wurtele, and P. Michel, "Holographic plasma lenses," Phys. Rev. Lett. **128**, 065003 (2022).

[32] Z. M. Sheng, K. Mima, J. Zhang, and H. Sanuki, "Emission of electromagnetic pulses from laser wakefields through linear mode conversion," Phys. Rev. Lett. **94**, 095003 (2005).

[33] B. Gonzalez-Izquierdo, R. J. Gray, M. King, R. J. Dance, R. Wilson, J. McCreadie, N. M. H. Butler, R. Capdessus, S. Hawkes, J. S. Green *et al.*, "Optically controlled dense current structures driven by relativistic plasma aperture-induced diffraction," Nat. Phys. **12**, 505–512 (2016).

[34] B. Gonzalez-Izquierdo, M. King, R. J. Gray, R. Wilson, R. J. Dance, H. Powell, D. A. Maclellan, J. McCreadie, N. M. H. Butler, S. Hawkes *et al.*, "Towards optical polarization control of laser-driven proton acceleration in foils undergoing relativistic transparency," Nat. Commun. **7**, 12891 (2016).

[35] V. A. Vshivkov, N. M. Naumova, F. Pegoraro, and S. V. Bulanov, "Nonlinear electrodynamics of the interaction of ultra-intense laser pulses with a thin foil," Phys. Plasmas **5**, 2727–2741 (1998).

[36] M. J. Duff, R. Wilson, M. King, B. Gonzalez-Izquierdo, A. Higginson, S. D. R. Williamson, Z. E. Davidson, R. Capdessus, N. Booth, S. Hawkes, D. Neely, R. J. Gray, and P. McKenna, "High order mode structure of intense light fields generated via a laser-driven relativistic plasma aperture," Sci. Rep. **10**, 105 (2020).

[37] L. Yi, "High-harmonic generation and spin-orbit interaction of light in a relativistic oscillating window," Phys. Rev. Lett. **126**, 134801 (2021).

[38] T. D. Arber, K. Bennett, C. S. Brady, A. Lawrence-Douglas, M. G. Ramsay, N. J. Sircombe, P. Gillies, R. G. Evans, H. Schmitz, A. R. Bell, and C. P. Ridgers, "Contemporary particle-in-cell approach to laser-plasma modelling," Plasma Phys. Controlled Fusion **57**, 113001 (2015).

[39] E. J. Dolier, M. King, R. Wilson, R. J. Gray, and P. McKenna, "Multi-parameter Bayesian optimization of laser-driven ion acceleration in particle-in-cell simulations," New J. Phys. (published online).

[40] R. A. Snavely, M. H. Key, S. P. Hatchett, T. E. Cowan, M. Roth, T. W. Phillips, M. A. Stoyer, E. A. Henry, T. C. Sangster, M. S. Singh *et al.*, "Intense high-energy proton beams from petawatt-laser irradiation of solids," Phys. Rev. Lett. **85**, 2945 (2000).

[41] S. C. Wilks, A. B. Langdon, T. E. Cowan, M. Roth, M. Singh, S. Hatchett, M. H. Key, D. Pennington, A. MacKinnon, and R. A. Snavely, "Energetic proton generation in ultra-intense laser–solid interactions," Phys. Plasmas **8**, 542–549 (2001).

[42] M. R. Siegrist, "Self-focusing in a plasma due to ponderomotive forces and relativistic effects," Opt. Commun. **16**, 402–407 (1976).

[43] T. Frazer, R. Wilson, M. King, N. Butler, D. Carroll, M. Duff, A. Higginson, J. Jarrett, Z. Davidson, C. Armstrong *et al.*, "Enhanced laser intensity and ion acceleration due to self-focusing in relativistically transparent ultrathin targets," Phys. Rev. Res. **2**, 042015 (2020).